RSC Advances

ROYAL SOCIETY OF CHEMISTRY

PAPER

View Article Online
View Journal | View Issue

Cite this: *RSC Adv.*, 2026, **16**, 453

Organoclay/functionalized-graphene dual-filler complex for high-performance polyimide nanocomposites

Jun Yeon Hwang,[a] Ae Ran Lim *[b] and Jin-Hae Chang *[c]

Aromatic polyimides (PIs) are super engineering polymers with excellent mechanical properties and thermal stability, making them suitable for applications in semiconductor devices, displays, and electronic materials. In this study, a poly(amic acid) (PAA) was synthesized from dianhydride 4,4′-biphthalic anhydride and diamine *N*,*N*′-[2,2′-bis(trifluoromethyl)-4,4′-biphenylene]bis(4-aminobenzamide) monomers, and a hybrid PAA was prepared by dispersing a complex filler using a solution intercalation method. The PAA hybrid solution was thermally imidized under various heat treatment conditions to obtain PI nanocomposite films. A novel complex filler containing both clay and graphene was synthesized through organic surface modification to improve compatibility and miscibility with the PI matrix. This dual-filler system was designed to enhance the overall performance of the PI hybrid films by exploiting the synergistic effects of both fillers. In this study, a C8-complex filler composed of octyl-modified montmorillonite and octyl-functionalized graphene was utilized. PI hybrid films were fabricated by dispersing the C8-complex filler into the PI matrix at various loadings ranging from 0 to 2.0 wt%. The effects of C8-complex filler content on the dispersion morphology, thermomechanical properties, and optical transparency of the resulting PI hybrid films were systematically investigated.

Received 26th October 2025
Accepted 18th December 2025

DOI: 10.1039/d5ra08198j

rsc.li/rsc-advances

1. Introduction

Polyimides (PIs) are high-performance polymers characterized by outstanding thermal stability, mechanical strength, and chemical resistance.[1–3] Synthesized *via* the polycondensation of aromatic dianhydrides and diamines, they typically exhibit high glass transition and decomposition temperatures, often exceeding 400 °C. These features enable their use in demanding applications such as aerospace, electronics, and automotive industries.[4,5] PIs also possess excellent electrical insulation, low dielectric constants, and strong resistance to solvents and radiation.[6] However, their rigid aromatic backbone often leads to poor solubility and limited processability. To overcome these drawbacks, structural modifications incorporating flexible linkages, bent configurations, or aliphatic units into the main chain have been investigated.[7] Colorless polyimides (CPIs) with such modified structures exhibit excellent optical transparency and flexibility, making them highly promising alternative materials to glass for next-generation flexible displays, transparent electronic devices, and semiconductor packaging substrates.[8–10] As such, PIs remain essential materials in advanced industrial applications requiring thermal and structural reliability.

The organoclay/functionalized-graphene (OC/FG) complex is a high-performance dual nanofiller system designed to enhance the overall properties of polymer nanocomposites by combining the unique advantages of both OC and FG. OCs, typically derived from layered silicates like montmorillonite (MMT), are surface-modified with organic cations (*e.g.*, alkylammonium salts) to improve compatibility and dispersion in polymer matrices.[11–13] FG produced by introducing polar groups such as amines or carboxyl groups onto the graphene surface, addresses the intrinsic aggregation tendency of pristine graphene, promoting stable dispersion and strong interfacial interactions with polymers.[14,15]

Polymer hybrids utilizing an OC/FG complex filler—synthesized by combining clay and graphene into a single hybrid system—represent a nanoscale filler that integrates two distinct hybrids with different properties to enhance the overall performance of polymeric materials. The OC used in this composite is an organically modified inorganic clay with a layered structure, in which the clay surface is functionalized with alkyl groups or similar moieties.[16] This modification improves compatibility with the polymer matrix and enhances filler dispersion. On the other hand, FG is graphene modified with functional groups such as amine or carboxyl groups on its surface.[17] These modifications help disperse the inherently

[a]*Institute of Advanced Composite Materials, Korea Institute of Science and Technology (KIST), Jeonbuk, 55324, South Korea*

[b]*Department of Science Education, Jeonju University, Jeonju 55069, South Korea. E-mail: arlim@jj.ac.kr*

[c]*Institute of Carbon Technology, Jeonju University, Jeonju 55069, South Korea. E-mail: changjinhae@hanmail.net*

aggregative graphene more stably within the polymer and strengthen interfacial interactions.

Each of these two fillers contributes its own advantages while compensating for the other's limitations. Within the polymer matrix, they form a complex nanostructure through hydrogen bonding, electrostatic interactions, and π–π stacking. This structure strongly interacts with the polymer chains, resulting in improved mechanical properties such as tensile strength, as well as enhanced thermal stability, electrical conductivity, and gas barrier properties. In particular, the high thermal conductivity of graphene and the layered structure of clay synergistically increase the glass transition temperature (T_g) and thermal decomposition temperature. The electrical conductivity of graphene also imparts electrical functionality to the composite.[18,19]

Moreover, OC helps prevent the aggregation of graphene, while graphene inhibits the restacking of clay platelets, thereby enhancing the overall dispersion of both fillers. This synergistic effect maximizes the composite's comprehensive physical properties and contributes to a more stable internal structure of the polymer hybrid.[20] Such hybrids, utilizing the synergistic effects of OC/FG complex fillers, are emerging as a promising technology for significantly advancing the properties of next-generation polymer materials.

PI hybrids incorporating an OC/FG complex offer the advantage of simultaneously dispersing two nanofillers with distinct properties, thereby significantly enhancing the overall performance of PI-based hybrids. These PI hybrids, enhanced through the dual filler approach, exhibit superior mechanical and thermal properties, electrical functionality, and barrier performance, making them suitable for a wide range of industrial applications.[21,22] In particular, when applied to CPI, the concentration and structure of the fillers can be precisely tuned to control transparency, color, and ultraviolet (UV) shielding capabilities, enabling their use in optical applications as well.

In addition to the previously discussed nanoclay and graphene, conventional reinforcing fillers such as carbon nanotubes (CNTs) and alumina have also been widely employed; however, their effectiveness is often limited by their tendency to agglomerate and the associated increase in brittleness. Accordingly, clay and graphene were selected in this study due to their high aspect ratios, favorable interfacial interactions, and ability to efficiently reinforce PI matrices even at low filler loadings.[23–26]

In this study, a new PI was synthesized using 4,4′-biphthalic anhydride (BPA) and *N*,*N*′-[2,2′-bis(trifluoromethyl)-4,4′-biphenylene] bis(4-aminobenzamide) (FPA). Hybrid films were fabricated by dispersing an appropriate amount (≤2 wt%) of filler into the synthesized PI, and the properties of the hybrid films were investigated according to the filler content. This paper presents a novel approach for synthesizing PI hybrids by utilizing the synergistic effect of dual fillers (OC/FG complex), deviating from the conventional method of employing clay and graphene as individual fillers in polymer nanocomposites. Specifically, a hybrid film was prepared by dispersing a complex filler composed of octylamine-modified MMT (C8-MMT) and octylamine-modified graphene sheets (C8-GS), collectively referred to as the C8-MMT/C8-GS (C8-Complex), into the matrix PI at the nanoscale.

The fabricated hybrid films were evaluated in terms of filler dispersion state, thermomechanical properties, and optical transparency as a function of the complex filler content. Furthermore, the optimal filler content was determined by analyzing the changes in the film properties.

The aim of this study was to obtain experimental data on the intermolecular interactions between the organic components of the complex fillers and the PI matrix polymer in the hybrid films, and to evaluate how changes in the filler content affect the overall properties of the PI hybrid films.

2. Experimental

2.1. Materials

All reagents for synthesizing PI, including BPA and FPA, were purchased from TCI (Tokyo, Japan) and Aldrich Chemical Co. (Yongin, Korea). Molecular sieves (4 Å) were used to remove moisture from the solvent DMAc. Na^+-MMT with a cation exchange capacity of 119 m eq per 100 g (ref. 27) was purchased from Aldrich (Yongin, Korea), and graphene oxide (GO) was purchased from Standard Graphene Co. (Ulsan, Korea).

2.2. Preparation of C8-MMT

Under a nitrogen atmosphere, octylamine (11.47 g) was dissolved in an HCl solution (4.8 mL of HCl in 100 mL of distilled water) and stirred at 80 °C for 1 h. Separately, Na^+-MMT (20 g) was dispersed in distilled water (400 mL) and stirred at 80 °C for 1 h. The two solutions were then combined and stirred vigorously at 80 °C for an additional 2 h. The resulting white solid was collected by vacuum filtration, washed with a 1 : 1 mixture of distilled water and ethanol (v/v), and freeze-dried under vacuum at room temperature for 24 h. The final yield of C8-MMT was approximately 92%.

2.3. Synthesis of the C8-MMT/C8-GS complex (C8-complex)

GO (1.0 g) was dispersed in distilled water (1 L) by stirring for 12 h, followed by sonication for 2 h. Separately, phosphotungstic acid (PTA, $H_3PW_{12}O_{40}$, 0.5 g) was dissolved in distilled water (30 mL) and stirred at room temperature for 1 h. The PTA solution was then added to the GO dispersion and stirred for 1 h. PTA releases oxonium ions (*e.g.*, H_3O^+, $H_5O_2^+$) in water, but its polyanionic clusters strongly interact with inorganic frameworks. In this system, PTA acted as a binder between MMT and GS, remaining stable within the hybrid matrix.[28,29]

In a separate beaker, C8-MMT (1.0 g) was dispersed in ethanol (30 mL) and sonicated for 1 h. This dispersion was added dropwise to the GO/PTA solution over 1–2 min under stirring, then stirred for 30 min. Octylamine (4.0 g), dissolved in ethanol (30 mL), was then added dropwise over 1–2 min, and the mixture was stirred for 1 h. The reaction mixture was further stirred vigorously at room temperature for 12 h. The resulting solid was collected by filtration, washed three times with ethanol (300 mL), and dried in a vacuum oven at 80 °C for 24 h to obtain the C8-complex.

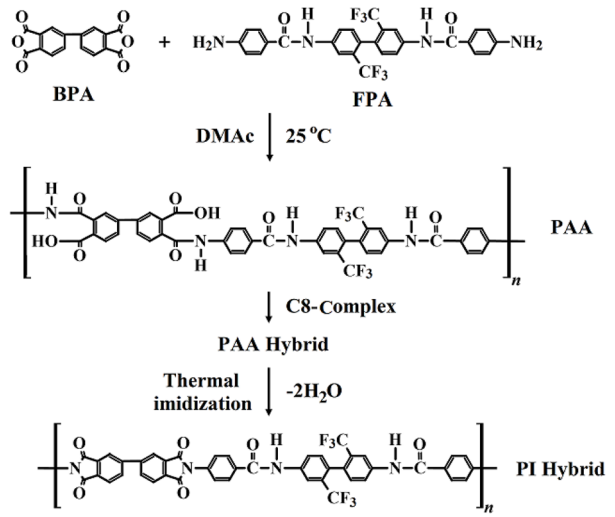

Scheme 1 Synthetic routes for PI hybrid.

2.4. Intercalation method of PI hybrid films containing the C8-complex

PI hybrid films were prepared *via* a solution intercalation method. The solution intercalation method is preferred for PI hybrid films because it enables uniform filler dispersion and strong interfacial interactions under mild conditions, while avoiding the processing limitations associated with melt blending and the complexity of *in situ* polymerization.[30]

Since all PI hybrid films in this study were fabricated using the same procedure, the synthesis of a representative hybrid film containing 1.0 wt% of the C8-complex is described here: The diamine monomer FPA (5.59 g, 1×10^{-2} mol) was dissolved in DMAc (40 mL) under stirring. After complete dissolution, the dianhydride monomer BPA (2.94 g, 1×10^{-2} mol) was added, and the mixture was stirred under a nitrogen atmosphere at room temperature for 16 h to form a poly(amic acid) (PAA) solution. The structures of the monomers and the detailed synthesis procedure are illustrated in Scheme 1. Separately, the C8-complex (0.08 g) was dispersed in DMAc (50 mL), then added to the PAA solution. The mixture was stirred under nitrogen at room temperature for 16 h, followed by additional stirring and sonication for 30 min. This dispersion and sonication process was repeated three times to ensure uniform mixing. The final solution was cast onto a glass plate and subjected to thermal imidization in a vacuum oven, using a stepwise heating schedule as outlined in Table 1.

2.5. Characterization

The structural, morphological, thermal, mechanical, and optical properties of the newly synthesized PI films were systematically characterized using a range of analytical techniques.

Fourier-transform infrared (FT-IR) spectroscopy (PerkinElmer L-300; London, UK) was employed to identify characteristic functional groups, confirming the successful formation of the PI structure. Spectra were collected over the range of 4000–1000 cm^{-1} with a resolution of 32 cm^{-1} and a scan speed of 0.2 cm s^{-1}. Additionally, solid-state ^{13}C cross-polarization/magic angle spinning nuclear magnetic resonance ^{13}C CP/MAS NMR) spectroscopy was conducted using a Bruker 400 DSX spectrometer (Berlin, Germany) operating at a Larmor frequency of 100.61 MHz to further verify the chemical structure.

The interlayer spacing of the dispersed fillers within the PI hybrid films was investigated using wide-angle X-ray diffraction (XRD; D/Max-IIIB, Tokyo, Japan) with a Ni-filtered Cu-Kα radiation source. Diffraction patterns were recorded at a scan rate of 2° min^{-1} over a 2θ range of 3–15°. The fracture surface morphology of the extruded films was examined *via* scanning electron microscopy (SEM; Hitachi S-2400, Tokyo, Japan) following gold sputter-coating to enhance surface conductivity. High-resolution transmission electron microscopy (HR-TEM; JEOL JEM-2100, Tokyo, Japan) operated at 120 kV was utilized to visualize the dispersion and morphology of the nanofillers within the polymer matrix. TEM specimens were prepared by embedding the films in epoxy resin, followed by ultrathin sectioning (90 nm) using a microtome under vacuum. Multiple magnifications were used to examine the same regions for consistency.

Thermal properties were evaluated using differential scanning calorimetry (DSC; Netzsch F3200, Munich, Germany) and thermogravimetric analysis (TGA; TA Q-500, New Castle, USA), performed at a heating rate of 20 °C min^{-1} under a nitrogen atmosphere (flow rate: 30 mL min^{-1}). The coefficient of thermal expansion (CTE) was determined by thermomechanical analysis (TMA; Seiko TMA/SS100, Tokyo, Japan) under a constant load of 0.1 N and a heating rate of 5 °C min^{-1}. CTE values were obtained during a second heating cycle from 50 °C to 230 °C to ensure measurement stability.

Mechanical properties, including ultimate tensile strength and elastic modulus, were assessed using a universal testing machine (UTM; Shimadzu AG-50KNX, Tokyo, Japan) at a crosshead speed of 5 mm min^{-1}. At least 10 specimens per sample were tested, with outliers excluded and the remaining results averaged. Measurement errors were controlled within ± 1 MPa for tensile strength and ± 0.05 GPa for modulus.

The optical transmittance and yellow index (YI) of the PI hybrid films were analyzed using a UV-vis spectrophotometer

Table 1 Heat treatment conditions of PI hybrid film

Sample	Temperature (°C)/time (hr)/pressure (Torr)
PAA	25/14/760 → 50/1/1 → 80/1/1
PI hybrid	110/0.5/1 → 140/0.5/1 → 175/0.5/1 → 195/1/1 → 220/1/1 → 235/2/1

(Shimadzu UV-3600, Tokyo, Japan) and a spectrocolorimeter (Konica Minolta CM-3600d, Tokyo, Japan), respectively.

3. Results and discussion

3.1. Morphology of nanofillers

Pristine clay and graphene possess a characteristic single-layer, plate-like morphology with an approximate thickness of 1 nm and exceptionally high surface areas of 760 $m^2 g^{-1}$ and 2630 $m^2 g^{-1}$, respectively.[17] When uniformly dispersed at the nanoscale within a polymer matrix, these nanofillers can significantly enhance the thermal and mechanical performance of the resulting nanocomposites.

In this study, the surface morphologies of unmodified clay and graphene sheets were examined using TEM (Fig. 1). However, due to their inherently low compatibility and poor dispersibility in polymer systems, pristine clays and graphene often lead to composites with suboptimal physical properties. To address these limitations, surface-modified fillers—such as OC and FG—are employed. These fillers are chemically tailored through organic reactions on their surfaces, which significantly enhances their dispersion and interfacial compatibility within the polymer matrix. As a result, the modified nanofillers can be homogeneously distributed without aggregation or phase separation, thereby markedly improving the overall performance of the nanocomposite materials.

Although graphene is a planar carbon allotrope with a nominal thickness of approximately 1 nm,[31–34] it often tends to aggregate into multilayered clusters. As a result, there is a significant discrepancy between the theoretical thickness and the actual thickness of FG used in practical applications, making precise thickness measurement critically important. In this study, the thickness of the synthesized C8-GS layers was examined using SEM at different magnifications. The measured thickness of the graphene layer was 3.53 nm (see Fig. 2). Considering that the thickness of pristine graphene is approximately 1 nm, this result confirms that octylamine was chemically grafted onto the surface of the graphene sheets.[35]

3.2. Schematic illustration and TEM image of the C8-complex

Fig. 3(I) presents a schematic illustration of the C8-complex, in which organically modified clay (C8-MMT) and C8-GS are interconnected *via* a phosphotungstic acid (PTA) binder.

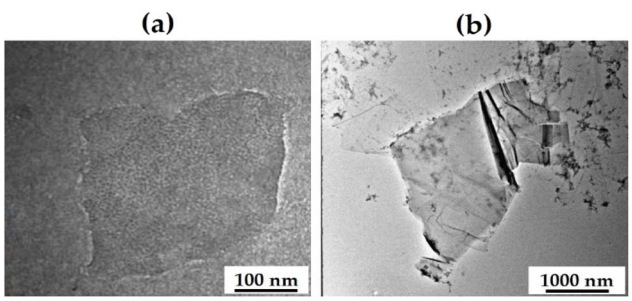

Fig. 1 TEM images of (a) pristine clay and (b) graphene sheet.

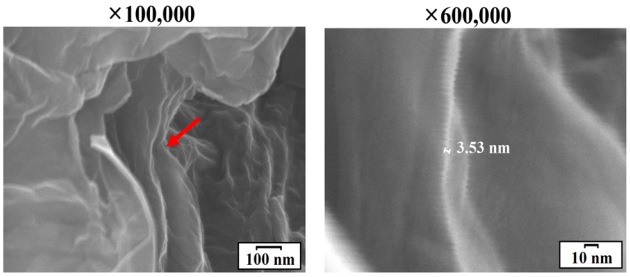

Fig. 2 SEM images of FG according to different magnifications.

Fig. 3(II) shows the TEM image of the C8-complex composed of both clay and graphene. In the TEM image, the overlapping dark regions correspond to (a) clay, while the transparent, gray-toned sheet structures represent (b) GSs.

The TEM images of MMT and graphene exhibit distinct differences in their structural characteristics. Specifically, MMT typically shows a well-defined layered structure, which appears as a series of dark, repeating lines in the TEM images. Due to this multilayered configuration, MMT forms stacked structures with low electron transparency (a), resulting in relatively dark contrast. In contrast, graphene appears as a transparent and thin sheet composed of one or a few atomic layers (b), and is generally observed in gray tones in TEM images.[35]

3.3. Structural analysis of PI using FT-IR and ^{13}C-NMR

Fig. 4 presents the functional groups within the PI structure as identified by FT–IR spectroscopy. In the FT-IR spectrum, an N–H stretching vibration was observed at 3323 cm^{-1}, while C═O stretching vibration bands appeared at 1786 cm^{-1} and 1715 cm^{-1}. Additionally, a characteristic peak corresponding to the C–N–C stretching vibration of the imide group was observed at 1369 cm^{-1}.[36] The presence of these imide functional groups confirms the successful formation of PI.

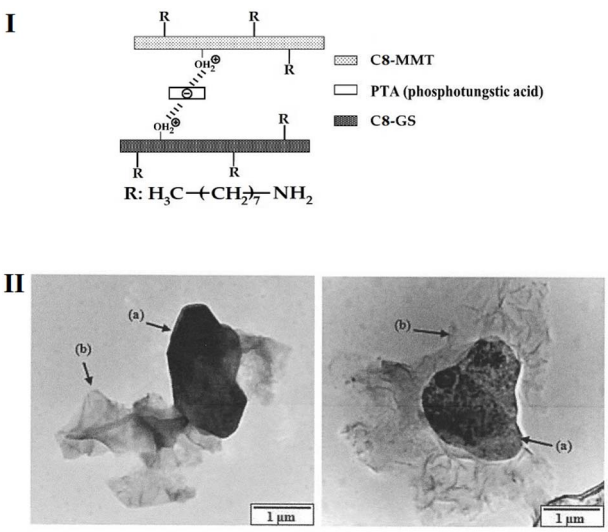

Fig. 3 Schematic illustration of the C8-complex filler using PTA as a binder (I). TEM micrograph of C8-complex: (a) clay and (b) graphene sheet (II).

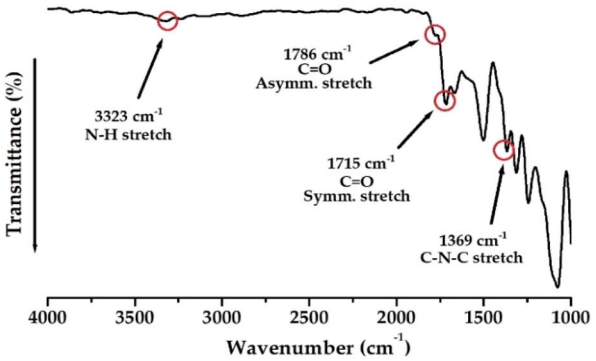

Fig. 4 FT-IR spectrum of PI.

To complement the FT–IR analysis, solid-state ^{13}C-NMR spectroscopy was employed to confirm the molecular structure of the synthesized solid PI by measuring the chemical shifts of carbon atoms. The chemical shifts of the ^{13}C-nuclei were calibrated to 0 ppm using the reference peak of tetramethylsilane at 25 °C. As shown in Fig. 5, the NMR peaks corresponding to phenyl carbons (a) and the carbons of $-CF_3$ substituents (b) were observed at 124.9 and 129.8 ppm, respectively, while additional peaks associated with imide and phenyl carbons appeared together at 132.5 ppm (c and d). The carbon atoms of the $-CF_3$-substituted benzene ring (e) were observed at 139.1 ppm, and the carbons of the C=O groups in the amide (f) and imide rings (g) were detected simultaneously at 165.9 ppm.[37] The experimentally determined structure of the PI synthesized in this study was consistent with the predicted molecular structure based on the FT-IR and ^{13}C-NMR analyses.

3.4. XRD patterns

The crystalline structure of the synthesized C8-complex was investigated by XRD analysis. This technique provided detailed information on the positions of the XRD peaks and the corresponding *d*-spacing values observed within the 2θ range of 3–15°. Fig. 6 presents the XRD patterns of the organo-modified fillers, the complex fillers derived from them, and the PI hybrid films containing various amounts of the complex fillers.

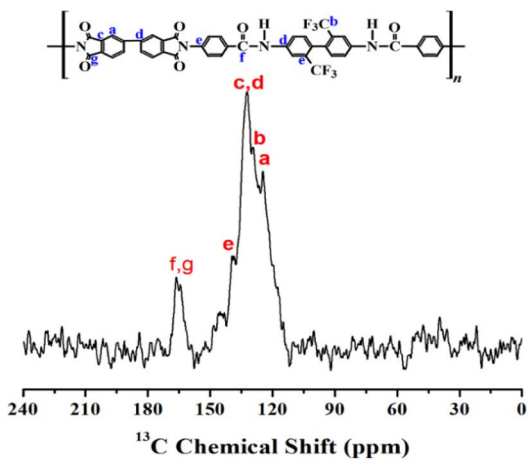

Fig. 5 ^{13}C-NMR chemical shifts of PI film.

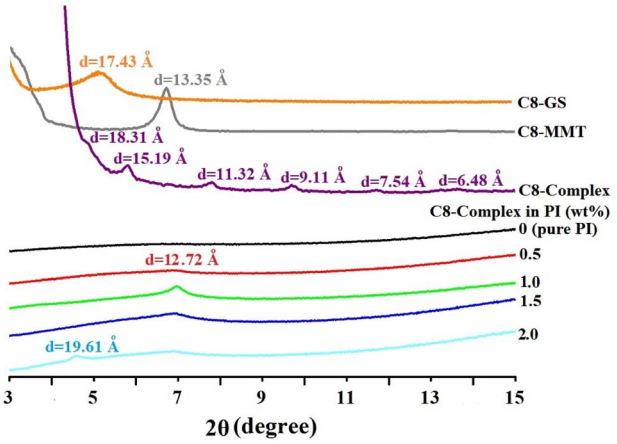

Fig. 6 XRD patterns of organically modified fillers and PI hybrid films containing various C8-complex contents.

Distinct peaks of C8-GS and C8-MMT were observed at $2\theta = 5.06°$ ($d = 17.43$ Å) and $2\theta = 6.61°$ ($d = 13.35$ Å), respectively.

For the C8-complex synthesized using C8-GS and C8-MMT, multiple peaks were detected within the 3–15° range. In particular, a small peak was observed at $2\theta = 4.82°$ ($d = 18.31$ Å), and multiple peaks appeared in the range between $2\theta = 5.81°$ ($d = 15.19$ Å) and 13.65° ($d = 6.48$ Å). As 2θ increased, the intensities of the resulting peaks gradually decreased, and each peak

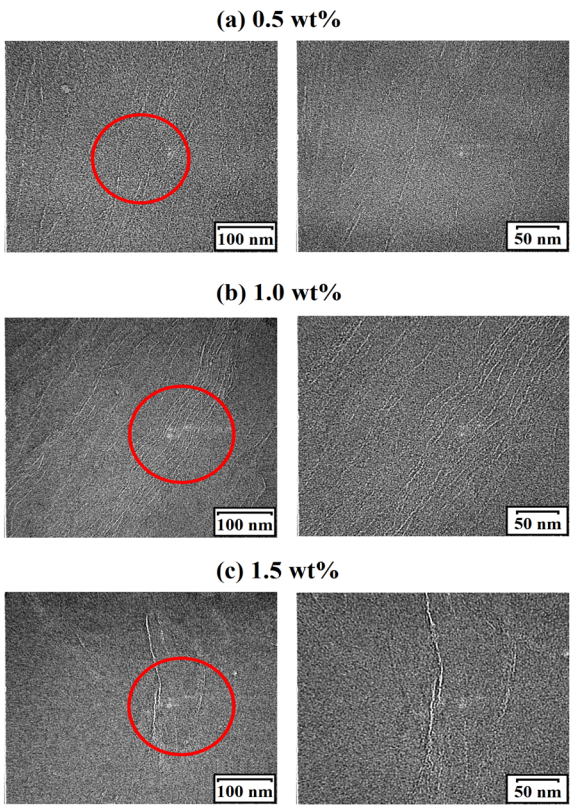

Fig. 7 TEM images of PI hybrids with various C8-complex contents of (a) 0.5 wt%, (b) 1.0 wt%, and (c) 1.5 wt%. The circled regions in all images on the left were magnified and are shown on the right.

exhibited a highly uniform 2θ spacing. For example, the 2θ values increased almost uniformly to 5.81° ($d = 15.19$ Å), 7.80° ($d = 11.32$ Å), 9.70° ($d = 9.11$ Å), 11.72° ($d = 7.54$ Å), and 13.65° ($d = 6.48$ Å), respectively. Such consistent spacing indicates that the clay/graphene complex nanofiller synthesized in this study possesses a well-ordered crystalline structure.

The XRD patterns of PI hybrid films containing different loadings of the C8-complex filler in the 2θ range of 3–15° are also shown in Fig. 6. In the hybrid containing 0.5 wt% of the C8-complex, a very weak peak appeared at $2\theta = 6.94°$ ($d = 12.72$ Å), and this peak was observed at the same position as the filler content increased to 2.0 wt%.

The XRD patterns of PI hybrid films containing different loadings of the C8-complex show a very weak diffraction peak at $2\theta = 6.94°$ ($d = 12.72$ Å), which remains at nearly the same position as the filler content increases up to 2.0 wt%, indicating that the average interlayer spacing of the C8-complex is largely preserved within the PI matrix. It should be noted that a constant peak position alone does not necessarily indicate filler aggregation, as it may also result from stable interlayer spacing or possible orientation effects, and the amorphous nature of the PI matrix together with weak diffraction intensity limits the reliability of XRD for directly assessing dispersion or aggregation.[38,39]

It should be noted that amorphous polymer matrices and exfoliated nanofillers do not always exhibit well-defined crystalline peaks that can be directly matched to joint committee on powder diffraction standards (JCPDS). Therefore, the XRD analysis was primarily interpreted by comparison with representative literature reports rather than exact JCPDS matching. This interpretation is consistent with previous studies on amorphous polyimides and exfoliated nanofillers, in which XRD patterns were analyzed based on broad peaks and comparison with the literature rather than exact matching with JCPDS data.[40–43]

At a higher filler loading 2.0 wt%, an additional diffraction peak at $2\theta = 4.50°$ ($d = 19.61$ Å) suggests an increased tendency toward local stacking of the filler layers, which is treated as a qualitative structural indication rather than independent evidence of aggregation. In contrast, TEM observations provide direct insight into the dispersion state, revealing relatively uniform dispersion at low filler loadings and the emergence of locally concentrated and stacked filler domains above a critical loading; therefore, conclusions regarding aggregation are primarily based on TEM results, with XRD serving as complementary structural information.

3.5. TEM photographs

While XRD analysis reveals information about the crystalline structure and interlayer spacing of nanofillers, TEM provides direct, high-resolution visualization of individual filler particles dispersed within the PI matrix. It is particularly effective for evaluating the nanoscale dispersion and layered structure of complex fillers.

Fig. 7 presents TEM images of PI hybrid films containing 0.5, 1.0, and 1.5 wt% of the C8-complex. In these images, the hair-like dark lines represent the individual layers of the nanofillers, typically around 1 nm thick.[17] The spaces between the lines correspond to the interlayer distances. To examine the dispersion state in more detail, the corresponding regions were magnified.

In the hybrid films containing 0.5 and 1.0 wt% of the C8-complex (Fig. 7a and b), the fillers are uniformly and finely dispersed throughout the matrix, with the filler domains maintained within a thickness of approximately 10–15 nm. However, at a higher filler content of 1.5 wt% (Fig. 7c), significant agglomeration occurs, with filler-layer domains thickening to 20–30 nm. This aggregation trend correlates well with the XRD results shown in Fig. 6, which also indicate a critical filler loading beyond which uniform dispersion is no longer maintained. Specifically, the TEM image of the 1.5 wt% sample reveals aggregated clusters of fillers, suggesting phase separation and non-uniform dispersion. These structural changes are further confirmed by the appearance of a new XRD peak at $2\theta = 4.50°$ ($d = 19.61$ Å), indicating the aggregation of excess fillers dispersed beyond the critical content.[44,45]

Together, the TEM and XRD analyses indicate that filler aggregation becomes prominent beyond a certain threshold concentration, disrupting the previously homogeneous filler distribution. Up to a content of 1.0 wt%, no major differences in the dispersion state were observed in either the XRD or TEM data. However, as filler content increases beyond this point, excessive loading leads to filler clustering, which negatively affects the thermomechanical properties and optical transparency of the hybrid films—a topic further discussed in later sections.

3.6. Thermal properties

The DSC results of PI hybrid films containing varying amounts of the C8-complex are summarized in Table 2, and the corresponding thermal curves obtained during the second heating cycle are presented in Fig. 8. The T_g of the pristine PI film was

Table 2 Thermal properties of PI hybrid films

C8-complex in PI (wt%)	T_g (°C)	T_D^{ia} (°C)	wt_R^{600b} (%)	CTE^c (ppm °C^{-1})
0 (pure PI)	240	472	77	7.0
0.5	243	435	77	7.2
1.0	245	420	75	9.9
1.5	263	417	75	10.1
2.0	274	394	76	12.0

[a] Initial decomposition temperature at 2% weight loss. [b] Weight residue at 600 °C. [c] Coefficient of thermal expansion for 2nd heating is 50–230 °C.

240 °C, and it gradually increased with increasing filler content from 0.5 to 2.0 wt%. For instance, at a C8-complex content of 0.5 wt%, the T_g increased to 243 °C, and further increased to 274 °C at 2.0 wt%. This T_g enhancement can be attributed to two main factors. First, the rigid and planar filler layers dispersed within the PI matrix reduce the free volume of the polymer chains. Second, the segmental motion of the polymer chains is hindered by the confinement effect induced by the interlayer dispersion between the rigid clay and graphene sheets.[46–48]

The initial decomposition temperature (T_D^i) indicates the onset of thermal degradation during heating, reflecting the temperature at which decomposition begins. It serves as an important parameter for evaluating the early-stage thermal stability and degradation behavior of a material. In general, fillers with high thermal stability, such as plate-like clays or graphene incorporated into composites, act as barriers that effectively block external heat transfer and reduce the volatilization of the PI matrix components at elevated temperatures. Therefore, when such thermally stable fillers are uniformly dispersed within the PI matrix, they suppress heat transfer and consequently contribute to an increase in the T_D^i.[49,50] However, contrary to theoretical expectations, the trend in TDi observed in this study showed the opposite tendency. That is, as the C8-complex content increased from 0 to 2.0 wt%, the T_D^i of the hybrid films gradually decreased from 472 °C to 394 °C, as shown in Table 2. This decline in T_D^i is ascribed to the presence of thermally unstable alkyl chains within the C8-complex. Therefore, a higher filler content introduces more alkyl contents with low thermal stability, leading to a decrease in the overall thermal stability of the PI hybrid films.[51,52]

Meanwhile, regardless of the filler content, the weight residue at 600 °C (wt_R^{600}) remained nearly constant in the range of 75–77%, as shown in Table 2. This observation indicates that the thermally labile organic moieties in the C8-complex are mostly decomposed near 600 °C, leaving behind thermally stable inorganic silicate and carbon residues within the hybrid system. The TGA thermograms of PI hybrid films containing various nanofiller contents are presented in Fig. 9.

In general, when a polymer film is heated, the polymer chains tend to relax in a direction perpendicular to the heating direction. However, in hybrid systems, the thermally stable and rigid planar structures of clay and graphene dispersed within the PI matrix restrict chain deformation, effectively suppressing thermal expansion by impeding heat transfer.[53,54] The CTE

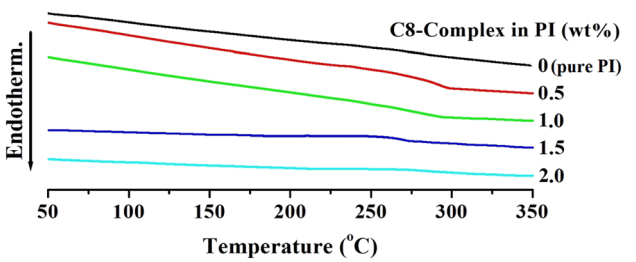

Fig. 8 DSC thermograms of PI hybrid films containing various C8-complex contents.

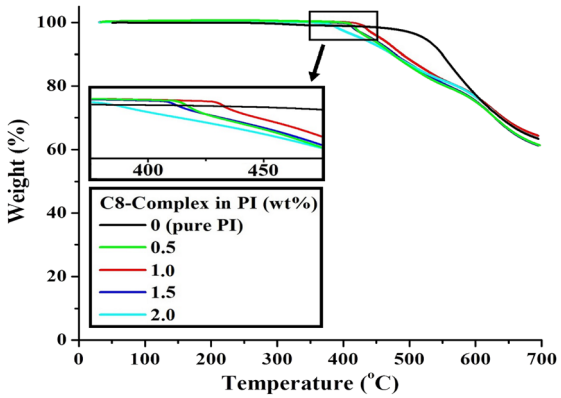

Fig. 9 TGA thermograms of PI hybrid films containing various C8-complex contents.

values for the PI hybrid films with varying filler contents are summarized in Table 2, and the corresponding TMA thermograms are shown in Fig. 10. As the C8-complex content increased from 0 to 2.0 wt%, the CTE values increased consistently from 7.0 to 12.0 ppm $°C^{-1}$. This trend contradicts the general expectation and can be explained by the increasing amount of thermally unstable alkyl groups in the filler, which leads to enhanced thermal expansion.

Based on these thermal property measurements, it can be concluded that the excellent barrier effect of the rigid and stiff clay and graphene dispersed within the PI matrix suppressed the segmental motion of the polymer chains located between the filler layers, thereby enhancing the thermal property (T_g). However, due to the presence of thermally unstable alkyl groups in the C8-complex, increasing the filler content led to a deterioration in the T_D^i and CTE in the hybrid films.[55,56]

3.7. Mechanical property

The ultimate tensile strength, initial modulus, and elongation at break (EB) of the pristine PI and PI hybrid films containing various amounts of dispersed complex filler were measured using a UTM, and the results are summarized in Table 3.

The ultimate tensile strength is influenced by factors such as the polymer chain structure, filler dispersion, interfacial

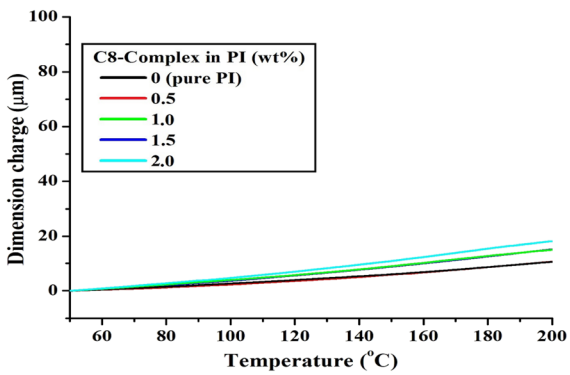

Fig. 10 TMA thermograms of PI hybrid films containing various C8-complex contents.

adhesion, crystallinity, and processing conditions.[57,58] The tensile strength increases when the polymer chains are linear and rigid, the crystallinity is high, and the fillers are uniformly dispersed with strong interfacial bonding to the polymer matrix. In contrast, excessive filler loading that leads to aggregation or poor interfacial adhesion can result in a reduction in tensile strength.

The ultimate tensile strength slightly increased from 68 MPa to 71 MPa as the filler content increased from 0 to 0.5 wt%, and further increased to a maximum of 78 MPa at a C8-complex content of 1.0 wt%. These results indicate that when the C8-complex filler, composed of rigid and plate-like clay and graphene, is uniformly dispersed in the PI matrix at low concentrations, it can effectively resist external tensile stress, resulting in enhanced mechanical strength of the hybrid films. However, when the filler content was increased to 2.0 wt%, the tensile strength drastically decreased to 18 MPa (see Table 3). When the C8-complex content exceeds a certain critical level, the filler tends to aggregate rather than disperse uniformly, leading to poor compatibility and dispersion within the polymer matrix. This, in turn, causes a significant reduction in tensile strength. Such aggregation behavior was clearly observed in the XRD and TEM images shown in Fig. 6 and 7.

The initial modulus represents the material's resistance to deformation under small applied stress and is primarily influenced by the rigidity of the polymer chains, the type and dispersion state of the filler, and the degree of crystallinity.[59,60] The initial modulus increases when the polymer chains are stiff and well-aligned, and when high-stiffness fillers are uniformly dispersed. Additionally, higher crystallinity enhances intermolecular interactions, thereby increasing resistance to initial deformation. However, similar to tensile strength, the initial modulus may decrease if an excessive amount of filler is added. The initial modulus exhibited a trend similar to that of the ultimate tensile strength (see Table 3). As the filler content increased from 0 to 1.0 wt%, the initial modulus increased from 2.63 GPa to 4.43 GPa. This enhancement is attributed to the complex filler composed of both clay and graphene aligning in the direction of the applied tensile force, due to its high stiffness and large aspect ratio.

Furthermore, this increase can also be explained by the restricted deformation of the PI chains caused by entanglement between the chains and the filler particles. However, when the filler content was increased to 2.0 wt%, the initial modulus decreased to 2.10 GPa, showing a trend consistent with that observed in the tensile strength results (Table 3). The changes in tensile strength and initial modulus of the PI hybrid films with varying C8-complex contents are presented in Fig. 11, confirming that the critical filler content for optimal mechanical properties is 1.0 wt%.

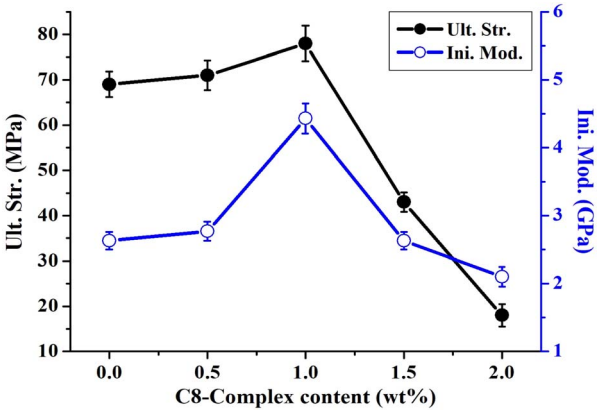

Fig. 11 Changes in the mechanical properties of PI hybrid films containing various C8-complex contents.

Organically modified fillers act as nucleating agents within the PI matrix, enhancing both the crystallinity and mechanical properties of the polymer. These fillers promote the alignment of polymer chains, leading to increased crystallinity, and simultaneously improve mechanical performance by effectively distributing external stress through strong interfacial interactions. Such changes in crystallinity contribute to the enhancement of tensile strength and modulus due to improved interfacial load transfer. However, when the filler content reaches 2.0 wt%, the mechanical properties tend to deteriorate because filler agglomeration disrupts the regular arrangement of the polymer chains.

The EB of the pristine PI film was 4%, and for the PI hybrid films, the EB remained consistently within the range of 4–5%, regardless of the filler content (see Table 3). These low EB values

Table 3 Mechanical properties of PI hybrid films

C8-complex in PI (wt%)	Ult. Str.[a] (MPa)	Ini. Mod.[b] (GPa)	E.B.[c] (%)
0 (pure PI)	68	2.63	4
0.5	71	2.77	5
1.0	78	4.43	5
1.5	43	2.63	4
2.0	18	2.10	4

[a] Ultimate strength. [b] Initial modulus. [c] Elongation at break.

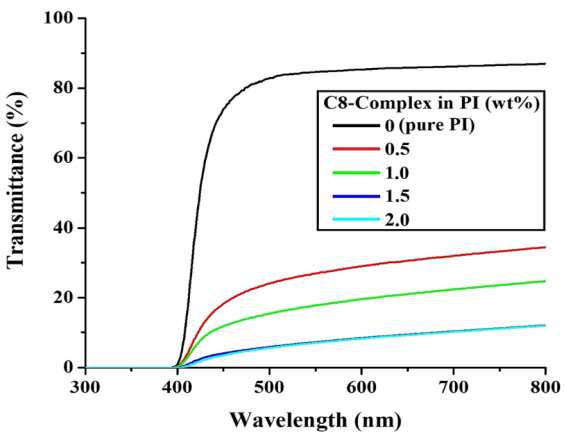

Fig. 12 UV-vis. Transmittances of PI hybrid films containing various C8-complex contents.

Table 4 Optical properties of PI hybrid films

C8-complex in PI (wt%)	Thickness[a] (μm)	λ_0[b] (nm)	500nm^{trans} (%)	YI[c]
0 (pure PI)	43	398	83	10
0.5	41	400	24	29
1.0	42	403	15	33
1.5	42	408	6	42
2.0	43	412	5	50

[a] Film thickness. [b] Cut-off wavelength. [c] Yellow index.

are attributed to the presence of brittle and inelastic inorganic components such as clay and graphene. Similar EB values have been reported in other hybrid materials containing such inorganic fillers.[61,62]

3.8. Optical transparency

The optical transparency of hybrid films is closely associated with the filler content and its degree of dispersion within the polymer matrix. When the filler content exceeds a critical threshold, the plate-like structures of clay and graphene tend to aggregate, obstructing the passage of light through the film and thereby decreasing transmittance. Conversely, if the fillers are uniformly exfoliated and dispersed at the nanoscale, the optical transparency of the hybrid films can be enhanced. Thus, the dispersion state of the hybrid fillers is directly correlated with the optical clarity of the resulting films.

The optical transparencies of the PI hybrid films were evaluated using UV-vis. Spectroscopy, and analyzed based on three key parameters: the cut-off wavelength (λ_o), transmittance at 500 nm (500 nm^{trans}), and YI. The UV-vis. Spectra of the PI hybrid films are presented in Fig. 12, and the corresponding values are summarized in Table 4. To minimize measurement errors, the film thickness was controlled within the range of 41–43 μm.

As the content of the C8-complex in the PI hybrid films increased up to 2.0 wt%, the λ_0 value gradually shifted from 398 nm to 412 nm, whereas the 500 nm^{trans} value dramatically decreased from 83% to 5%. This change in transmittance is attributed to the formation of layered structures by clay and graphene fillers, which increasingly scatter light as their concentration rises.

In addition, the YI values were strongly influenced by the content of the composite filler. As shown in Table 4, the YI of the neat PI film was 10, but it increased significantly to 50 as the filler content rose from 0 to 2.0 wt%. Representative photographs of the neat PI and PI hybrid films with varying C8-complex contents are provided in Fig. 13. With increasing filler content, the hybrid films exhibited progressively darker coloration, and at 2.0 wt%, the film appeared completely black, rendering the printed logo underneath unreadable and indicating a complete loss of optical transparency. In particular, the reason why the films exhibited a markedly darker color even at low filler contents in this study is mainly attributed to the inherent black color of graphene.

The deterioration of optical transparency in PI hybrid films with increasing organically modified filler content can be attributed to several factors. Specifically, the filler particles may scatter incident light, reducing clarity; excessive filler content can also lead to agglomeration, forming visible domains. Furthermore, poor compatibility between the fillers and the polymer matrix may result in interfacial inhomogeneity, adversely affecting light transmittance. Consequently, due to these combined effects, the optical transparency of the films decreases with increasing filler content.[63]

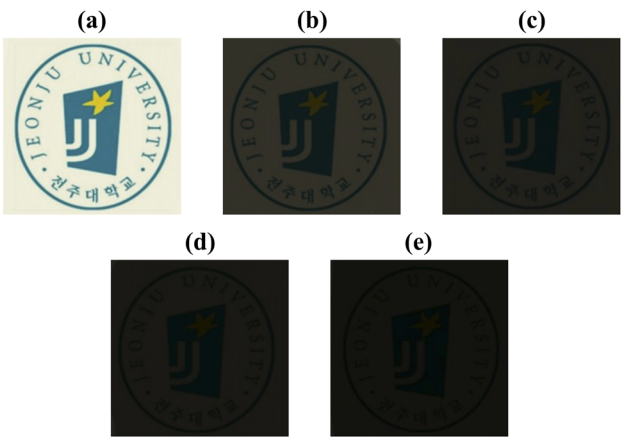

Fig. 13 Photographs of PI hybrid films with various C8-complex contents. (a) 0 (pure PI), (b) 0.5, (c) 1.0, (d) 1.5, and (e) 2.0 wt% C8-complex.

4. Conclusions

While numerous previous studies have fabricated polymer nanocomposites using either clay or graphene as individual fillers, this study introduces a novel approach by synthesizing a hybrid filler that simultaneously incorporates both clay and graphene. PI nanocomposite films were fabricated using this dual filler, referred to as the C8-complex, and the synergistic effects of the combined fillers on the resulting hybrid properties were systematically investigated.

In this work, PI hybrid films were prepared *via* a solution intercalation method using various concentrations of the newly synthesized C8-complex. The influence of filler content on the dispersion state, thermomechanical properties, and optical transparency of the resulting films was comprehensively evaluated. As the filler content increased to 2.0 wt%, the T_g improved, whereas both the T_D^i and CTE gradually deteriorated. In terms of mechanical properties, tensile strength and modulus increased with filler content up to a critical threshold, beyond which further addition of filler led to deterioration.

Optical transparency, however, steadily declined with increasing filler content.

These results suggest that nanoscale dispersion of the filler, while maintaining good interfacial adhesion with the polymer matrix, is crucial for achieving hybrid films with superior properties that are difficult to obtain through conventional fabrication methods. When the filler is uniformly distributed within the matrix at an optimal content (critical loading), the overall performance of the PI hybrid films can be significantly enhanced. Owing to these improved properties, the developed PI hybrid materials exhibit strong potential for application in advanced semiconductor and electronic film technologies. In addition to electronic films, PI nanocomposites have potential applications in aerospace and automotive insulation, optical protection layers, energy-related substrates, and high-performance barrier films, owing to their combined thermal stability, mechanical strength, and optical transparency.

Author contributions

J.-H. Chang and A. R. Lim designed the project and wrote the manuscript. J. Y. Hwang prepared the samples and participated in the data analysis. All authors have read and agreed to the published version of the manuscript.

Conflicts of interest

There are no conflicts to declare.

Data availability

The datasets used and/or analyzed during the current study available from the corresponding author on reasonable request.

Acknowledgements

This research was supported by the Regional Innovation System & Education (RISE) program through the Jeonbuk RISE Center, funded by the Ministry of Education (MOE) and the Jeonbuk State, Republic of Korea (2025-RISE-13-JJU).

References

1 R. J. Iredale, C. Ward and I. Hamerton, *Prog. Polym. Sci.*, 2017, **69**, 1–21.
2 Li. Gouzman, E. Grossnab, R. Verker, N. Atar, A. Bolker and N. Eliaz, *Adv. Mater.*, 2019, **31**, 1807738–1807752.
3 J. Shu, Z. Zhou, H. Liang and X. Yang, *Nanoscale Adv.*, 2024, **6**, 4309–4324.
4 V. Daghigh, H. Daghigh and R. Harrison, *J. Compos. Sci.*, 2025, **9**(10), 526.
5 D.-L. Liaw, K.-L. Wang, Y.-C. Huang, K.-R. Lee, J.-Y. Lai and C.-S. Ha, *Prog. Polym. Sci.*, 2012, **37**, 907–974.
6 Y. Y. Liu, J.-H. Cao, Y. Wang, S.-G. Shen, W.-H. Liang and D.-Y. Wu, *ACS Appl. Polym. Mater.*, 2022, **4**, 7664–7673.
7 L. K. Kwac, B.-J. Kim and J.-H. Chang, *RSC Adv.*, 2025, **15**, 29013–29022.
8 M. Zhang, J. Miao, Y. Xu, Z. Wang and J. Yan, *Macromolecules*, 2022, **55**, 7992–8001.
9 A. I. Barzic, R. M. Albu, I. Stoica, C. D. Varganici and C. Hulubei, *Polym. Bull.*, 2023, **80**, 4503–4522.
10 Z. Wang, Z. He, X. Ren, Y. Zhang, X. Wang, C. Yang, S. Han, H. Yu and J. Liu, *J. Appl. Polym. Sci.*, 2024, **141**, e55606.
11 S. J. Lee, M. Y. Choi, L. K. Kwac, H. G. Kim and J.-H. Chang, *Rev. Adv. Mater. Sci.*, 2023, **62**, 20230120.
12 E. J. Baileym and K. I. Winey, *Prog. Mater. Sci.*, 2020, **105**, 101242.
13 M. H. Nazari, Y. Zhang, A. Mahmoodi, G. Xu, J. Yu, J. Wu and X. Shi, *Prog. Org. Coat.*, 2022, **162**, 106573.
14 H. I. Shin and J.-H. Chang, *Polymers*, 2020, **12**, 135–152.
15 J. M. Garcia-Martinez, O. Laguna, S. Areso and E. P. Collar, *J. Polym. Sci. Part B: Polym. Phys.*, 2000, **38**, 1564–1574.
16 W. F. Jaynes and J. M. Bingham, *Clays Clay Miner.*, 1987, **35**, 440–448.
17 S. J. Lee, M. Y. Choi, L. K. Kwac, H. G. Kim and J.-H. Chang, *Polymers*, 2022, **14**, 2469.
18 F. Gao, *Mater. Today*, 2004, **7**, 50–55.
19 M.-S. Cao, X.-X. Wang, M. Zhang, W.-Q. Cao, X.-Y. Fang and J. Yuan, *Adv. Mater.*, 2020, **32**, 1907156.
20 A. Esfandiari, H. Nazokdast, A.-S. Rashidi and M.-E. Yazdanshenas, *J. Appl. Sci.*, 2008, **8**, 545–561.
21 L. Zuo, W. Fan, Y. Zhang, L. Zhang, W. Gao, Y. Huang and T. Liu, *Compos. Sci. Technol.*, 2017, **139**, 57–63.
22 J. Longun, G. Walker and J. O. Iroh, *Carbon*, 2013, **63**, 9–22.
23 X. Cui, G. Zhu and W. Liu, *Plast. Rubber Compos.*, 2016, **45**, 294–299.
24 N. Veeramani, D. R. Kumar, N. T. Manikandanath, A. S. Ganesh, S. Siju and G. J. Srinivas, *Polym. Res.*, 2024, **31**, 1–11.
25 A. R. Ashraf, Z. Akhter, M. A. Farid, L. C. Simon, K. Mahmood and M. F. Nazar, *Front. Mater*, 2025, **12**, 1504965.
26 V. Naveen, A. P. Deshpande and S. Raja, *RSC Adv.*, 2020, **10**, 33178–33188.
27 G. Lagaly, *Appl. Clay Sci.*, 1999, **15**, 379–395.
28 I. Honma, S. Nomura and H. Nakajima, *J. Membr. Sci.*, 2001, **185**, 83–94.
29 Y. Yu, X. Zhong, H. Su and A. Serra, *Polymer*, 2010, **51**, 1563–1571.
30 D. R. Paul and L. M. Robeson, *Polymer*, 2008, **49**, 3187–3204.
31 E. A. H. Segovia, D. Torres, J. R. P. Higareda and A. García, *Mech. Mater*, 2021, **158**, 103875.
32 N. Parvin, V. Kumar, S. W. Joo, S.-S. Park and T. K. Mandal, *Polymers*, 2022, **11**, 3345.
33 M. K. Bayazit, *ACS Omega*, 2023, **8**, 41273–41281.
34 Z. Xiong, *et al.*, *Nat. Commun.*, 2024, **15**, 55131.
35 A. Ali, F. Rehman, M. A. Khan, F. H. Memon, F. Soomro, M. Iqbal, J. Yang and K. H. Thebo, *ACS Omega*, 2022, **7**, 32410–32417.
36 D. L. Pavia, G. M. Lampman, G. S. Kriz and J. A. Vyvyan, *Introduction to Spectroscopy*, Cengage Learning, Boston, Massachusetts, USA, 2008, pp. 14–95.
37 D. L. Pavia, G. M. Lampman, G. S. Kriz and J. A. Vyvyan, *Introduction to Spectroscopy*, Cengage Learning, Boston, Massachusetts, USA, 2008, pp. 146–183.

38 S. S. Ray and M. Okamoto, *Prog. Polym. Sci.*, 2003, **28**, 1539–1641.
39 M. Y. Choi, A. R. Lim and J.-H. Chang, *RSC Adv.*, 2025, **15**, 15178–15189.
40 J. Ma, X. Liu, R. Wang, C. Lu, X. Wen and G. Tu, *Nanomaterials*, 2023, **13**, 656.
41 G. Geng, P. Chen, B. Guan, Y. Liu, C. Yang, N. Wang and M. Liu, *RSC Adv.*, 2017, **7**, 51838–51846.
42 J. Song, L. Xu, R. Xing, Q. Li, C. Zhou, D. Liu and H. Song, *Sci. Rep.*, 2014, **4**, 7515.
43 G. Vignesh, P. Devendran, N. Nallamuthu and S. Sudhahar, *J. Mater. Sci.: Mater. Electron.*, 2023, **34**, 820.
44 D. E. Abulyazied and A. Ene, *Polymers*, 2021, **13**(24), 4401.
45 J. Zhao, A. B. Morgan and J. D. Harris, *Polymer*, 2005, **23**, 8641–8660.
46 G. Zhu, H. Lao, F. Feng, M. Wang, X. Fang and G. Chen, *Eur. Polym. J.*, 2022, **179**, 111558.
47 L. Jiao, F. Luo, Z. Du, X. Dai, J. Mu, H. Wang, Z. Dong and X. Qiu, *React. Funct. Polym.*, 2022, **181**, 105449.
48 X. Ma, F. Zheng, C. G. C. E. van Sittert and Q. Lu, *J. Phys. Chem. B*, 2019, **123**, 8569–8579.
49 U. Min, J.-C. Kim and J.-H. Chang, *Polym. Eng. Sci.*, 2011, **51**, 2143–2150.
50 F. Liu, Z. Liu, S. Gao, Q. You, L. Zou, J. Chen, J. Liu and X. Liu, *RSC Adv.*, 2008, **8**, 19034–19040.
51 M. Villanueva, P. Vallet, T. Teijeira, A. Santiago-Alonso, A. Amigo, E. Tojo, L. M. Varela, J. J. Parajó, J. Salgado and J. Therm, *Analy. Calori.*, 2025, **150**, 6851–6861.
52 W. Peng, J. Xiong, T. Chen, D. Zhao, J. Liu, N. Zhang, Y. Teng, J. Yu and W. Zhu, *RSC Adv.*, 2024, **14**, 8081–8089.
53 H. Wu and L. T. Drzal, *Mater. Chem. Phys.*, 2014, **146**, 26–36.
54 G. Örçen and D. Bayram, *J. Mater. Sci.*, 2024, **59**, 3467–3487.
55 A. G. Khina, D. P. Bulkatov, I. P. Storozhuk and A. P. Sokolov, *Polymers*, 2025, **17**, 3097.
56 L. Meunier, D. Montarnal, D. Fournier, V. Gaucher, S. Duquesne and F. Samyn, *Polymer*, 2024, **290**, 126559.
57 A. U. Kini, M. Shettar, M. C. Gowrishankar and S. Sharma, *Cogent Eng.*, 2023, **10**, 2257949.
58 Y. Na, L. K. Kwac, H. G. Kim, Y. L. Joo and J.-H. Chang, *RSC Adv.*, 2023, **13**, 16285–16292.
59 D. S. Yoon, J. K. Choi and B. W. Jo, *Polymer*, 2010, **34**, 326–332.
60 M. Y. Choi, S. J. Lee, A. R. Lim and J.-H. Chang, *Sci. Rep.*, 2022, **12**, 20892.
61 S. Morimune-Moriya, M. Kotera and T. Nishino, *Polymer*, 2022, **256**, 125202.
62 K. H. Dehnou, G. S. Norouzi and M. Majidipour, *RSC Adv.*, 2023, **13**, 3976–4006.
63 M. Tawfilas, G. B. Torres, R. Lorenzi, M. Saibene, M. Mauri and R. Simonutti, *ACS Omega*, 2024, **9**, 29339–29349.